


Effect of low-mass galaxy interactions on their star formation

Smitha Subramanian¹, Chayan Mondal², and Venu Kalari³

¹ Indian Institute of Astrophysics, Koramangala II Block, Bangalore 560034, India
e-mail: smitha.subramanian@iiap.res.in

² Inter-University Centre for Astronomy and Astrophysics, Ganeshkhind, Post Bag 4, Pune 411007, India

³ Gemini Observatory, NSF NOIRLab, Casilla 603, La Serena, Chile

Received 30 March 2023 / Accepted 29 August 2023

ABSTRACT

According to the Λ cold dark matter model of galaxy formation, the hierarchical assembly process is scale-free and interactions between galaxies in all mass ranges are expected. The effects of interactions between dwarf galaxies on their evolution are not well understood. In this study, we aim to understand the effect of low-mass galaxy interactions on their star formation rate (SFR). We estimated the SFR of 22 interacting and 36 single gas-rich dwarf galaxies in the Lynx-Cancer void region using their far-ultraviolet (FUV) images from the GALEX mission. We find an enhancement in SFR by a factor of 3.4 ± 1.2 for interacting systems compared to single dwarf galaxies in the stellar mass range of 10^7 – $10^8 M_{\odot}$. Our results indicate that dwarf–dwarf galaxy interactions can lead to an enhancement in their SFR. These observations are similar to the predictions based on the simulations of dwarf galaxies at lower redshifts. Future deeper and higher-spatial-resolution UV studies will help us to understand the effect of dwarf galaxy interactions on the spatial distribution of star forming clumps and to identify star formation in tidal tails.

Key words. galaxies: dwarf – galaxies: interactions – galaxies: star formation – ultraviolet: galaxies

1. Introduction

One of the key drivers of galaxy evolution is the interaction between galaxies. Galaxy interactions can be broadly classified into two: mergers and fly-bys. Depending on the mass ratio of the interacting systems, they are again subclassified as minor (stellar mass ratio $<1:4$) and major (stellar mass ratio $>1:4$) interactions. These events in the high mass regime (stellar mass $>10^{10} M_{\odot}$) are relatively well studied in the local Universe, both observationally (Barton et al. 2000; Ellison et al. 2010; Woods et al. 2010; Patton et al. 2011, 2013, 2016; Scudder et al. 2012; Cao et al. 2016; Huertas-Company et al. 2016; Bickley et al. 2022; Shah et al. 2022) and theoretically (Toomre & Toomre 1972; Hernquist 1989; Barnes & Hernquist 1991; Mihos & Hernquist 1994a,b, 1996; Di Matteo et al. 2007; Torrey et al. 2012; Hopkins et al. 2013; Moreno et al. 2019; Padmanabhan & Loeb 2020; Patton et al. 2020; Brown et al. 2023; Byrne-Mamahit et al. 2023 and references therein). These studies show that the interactions between massive galaxies induce morphological changes (converting disc galaxies to spheroids), create stellar and gaseous streams around the galaxies, trigger star formation, and induce gas inflows leading to nuclear starburst and AGN activity. Similar studies of low-mass (stellar mass $<10^{10} M_{\odot}$) systems are relatively few, and most have focused on individual systems (Martínez-Delgado et al. 2012; Rich et al. 2012; Paudel et al. 2015; Annibali et al. 2016; Privon et al. 2017) and numerous panchromatic surveys, which studied dwarf galaxies, did not focus on the impact of interactions on their evolution. Observational studies are also limited due to the challenges in detecting these galaxies and the substructures around them. On the theoretical side, challenges exist in simulating large volumes to provide a realistic cosmological context while simultaneously resolving galaxies down to the dwarf regime.

According to the Λ cold dark matter (CDM) model of galaxy formation, the hierarchical assembly process is scale-free and interactions between galaxies in all mass ranges are expected. Observations show that dwarf galaxies are often found in associations (Tully et al. 2006; Bellazzini et al. 2013) and cosmological simulations predict that subhalos are often accreted in small groups (Li & Helmi 2008). This could explain the association of some of the Milky Way satellites with the plane of the orbit of the Magellanic Clouds (D’Onghia & Lake 2008; Kroupa et al. 2015) and point to a scenario of Magellanic group infall onto the Milky Way. Dwarf galaxies are the dominant galaxy population at all redshifts (Grazian et al. 2015) and the majority of mergers are expected to be between them (Fakhouri et al. 2010). Again, as low-mass galaxies have low tidal effects, it is not clear whether their interactions can induce star formation and morphological changes as observed for interacting massive galaxies. These objects are also more prone to environmental effects than massive galaxies (Venhola et al. 2019; Higgs & McConnachie 2021 and references therein). It is therefore essential to understand the effect of low-mass galaxy interactions on their evolution. Presently, there are dedicated ongoing and planned surveys to study dwarf galaxy assembly processes in the nearby Universe (Stierwalt et al. 2015; Higgs et al. 2016; Carlin et al. 2016; Annibali et al. 2020). With improved cosmological simulations now available (Dubois et al. 2021; Martin et al. 2021), we can compare the observed properties with predictions from simulations of dwarf galaxies.

Stierwalt et al. (2015) found an enhancement in star formation rates (SFRs) by a factor of 2.3 in isolated paired dwarfs (with pair separation <50 kpc, mass ratio of the pair <10 and pair member masses in the range 10^7 – $10^{9.7} M_{\odot}$, with a median mass of $10^{8.9} M_{\odot}$) over isolated single dwarfs of similar stellar mass. For one interacting pair of dwarfs (dm1647+21, with enhanced star formation, in the sample of Stierwalt et al. 2015),

Privon et al. (2017) found that the star formation is widespread and clumpy in contrast to merging massive galaxies, where gas funnelling leads to nuclear starburst. Studies by Lelli et al. (2014) and Kado-Fong et al. (2020) found that the presence of tidal features correlates with star formation activity. Sun et al. (2020) explored the environmental influences on the SFR of low-mass galaxies (with stellar masses in the range 10^8 – $10^{10} M_{\odot}$, with a median mass of $10^{9.5} M_{\odot}$ at redshift <0.07) using the SDSS-IV/MaNGA Integral Field Unit (IFU) data. These authors found an enhancement in the SFR of pairs (with pair separation of <100 kpc, mass ratio of the pair of <4 , and a line-of-sight kinematic separation of $\leq 100 \text{ km s}^{-1}$) in their inner regions, decreasing radially outwards. All these studies suggest that interactions on smaller scales have a role in triggering star formation and the spatial distribution of triggered star formation is significantly different from what is observed in interacting massive galaxies. Paudel et al. (2018) presented a catalogue of 177 interacting dwarfs with stellar mass of $<10^{10} M_{\odot}$ and redshifts of <0.02 (with a median mass of $10^{9.1} M_{\odot}$ and median redshift of 0.01). These authors found that dwarf–dwarf interactions tend to prefer the low-density environment. However, Paudel et al. (2018) did not find any enhancement in the star formation of interacting dwarfs compared to the star forming galaxies of the Local Volume. They also note that they mainly compiled their comparison sample data from the literature, and therefore their comparative study may not be as rigorous as that of the comparative study provided by Stierwalt et al. (2015) between interacting dwarf and non-interacting dwarf galaxies. As described above, the median stellar mass of the sample of galaxies analysed in all these previous studies is $\sim \geq 10^9 M_{\odot}$, which is the upper end of the low-mass regime. Therefore studies of more galaxies in different mass ranges are required. Studies of star formation in a carefully selected sample of interacting and non-interacting low-mass galaxies (in different mass ranges) in low-density environments will help us to understand the effect of dwarf–dwarf interactions on their star formation properties.

There are regions of low matter density in the Universe, known as voids. Surrounded by walls and filaments, voids are prominent features of the cosmic web and contain fewer galaxies. Numerical simulations as well as observations suggest that bluer dwarf galaxies with high specific SFRs (sSFRs) dominate the interior of these void regions (Rojas et al. 2005; Liu et al. 2015). Though voids are low-density regions, they are not devoid of structures. There are subvoids within voids, which are surrounded by walls and filaments that are relatively high-density regions (Aragon-Calvo & Szalay 2013). The structure formation within voids is similar to the early stages of structure formation in the low-density Universe. Therefore, dwarf galaxies in voids provide an opportunity to study galaxy interactions and assembly processes on small scales. In this context, we aim to study the instantaneous SFR of interacting dwarf galaxies (stellar masses in the range of 10^6 – $10^9 M_{\odot}$ with a majority of them in the mass range of 1 – $10 \times 10^7 M_{\odot}$) and make a comparison with the instantaneous SFR of the isolated single dwarf galaxies (with similar stellar masses) in the Lynx-Cancer void region using the GALEX far-ultraviolet (FUV) data in order to understand the effect of dwarf–dwarf interactions on their star formation properties.

The Lynx-Cancer void is located at the edge of the Local Volume at a distance of ~ 18 Mpc. Its proximity allows us to study low-mass galaxies. Galaxies in this void tend to be metal deficient compared to galaxies in higher-density environments, and this particular void hosts some of the most metal-poor and gas-rich dwarf galaxies known (Chengalur & Pustilnik

2013; Izotov & Thuan 2009; Pustilnik & Tepliakova 2011; Pustilnik et al. 2016). This suggests that these galaxies are relatively unevolved systems that may resemble galaxies in the early Universe. The study of such metal-poor, gas-rich, and interacting dwarf systems in this region will allow us to constrain interactions between small, high-redshift systems, which form the basis of the hierarchical galaxy assembly process.

In the following section, we define the sample and data. In Sects. 3 and 4, we present data analysis, our results and a discussion. We summarise our findings in Sect. 5.

2. Sample and data

We used a catalogue of dwarf galaxies in the Lynx-Cancer void region, provided by Pustilnik & Tepliakova (2011). The catalogue consists of 79 galaxies, including 75 dwarf galaxies ($-11.9 > M_B > -18.0$) and 4 sub-luminous galaxies ($-18.0 > M_B > -18.4$). This catalogue is nearly complete to $M_B < -14$ mag but misses some of the faint low-surface-brightness (LSB) galaxies. According to Pustilnik & Tepliakova (2011), there could be approximately 25–30 objects missing in the magnitude range of $-12.0 > M_B > -13.5$ mag. The main observational parameters of these galaxies taken from the literature are also provided in the catalogue. None of these galaxies are found to have any massive or luminous ($M_B < -19$) neighbouring galaxy within a 3D distance of 2 Mpc. The sample includes nine pairs of dwarf galaxies and six single galaxies with tidal tails, suggesting their interacting nature. The authors classified these 24 galaxies ($9 \times 2 + 6$) as interacting either based on the presence of a common HI envelope around two nearby galaxies in HI maps and/or indications of perturbed morphology in the HI maps and/or optical images. The pairs have a typical projected distance separation of several tens of kiloparsecs. The isolated single dwarf galaxies (55/79) are those with no nearby dwarf galaxies and with no significant distortions indicating any past interaction.

The photometric properties of these sample galaxies are estimated and tabulated by Perepelitsyna et al. (2014). These authors used the SDSS images of the sample galaxies in u, g, r, i bands and estimated the integrated magnitudes and colours. The B band magnitudes are also estimated from the g, r magnitudes and the corresponding transformation equations. From the B -band surface brightness profiles, the authors estimated the optical and Holmberg radii (corresponding to the B -band surface brightness levels of $25 \text{ mag arcsec}^{-2}$ and $26.5 \text{ mag arcsec}^{-2}$ respectively), the effective radii, and the observed ellipticity (semi-minor axis/semi-major axis, b/a) of each galaxy. From the integrated magnitudes, Perepelitsyna et al. (2014) also estimated the stellar mass of these galaxies using the mass–luminosity–colour relations (g band luminosity and $(g - i)$ colour) given by Zibetti et al. (2009). We note such stellar mass estimations are valid for diverse galaxy populations, including LSB dwarf galaxies (Du et al. 2020). As SFR varies as a function of stellar mass, comparison of SFR between the interacting and isolated galaxies in our sample should be performed for those in similar stellar mass bins. Therefore, galaxies without stellar mass estimates are removed from our further analysis. Of the 79 galaxies in the catalogue by Pustilnik & Tepliakova (2011), only 64 galaxies have stellar mass estimates from Perepelitsyna et al. (2014), as the remaining 15 galaxies are outside the SDSS footprint used to obtain multi-band photometry and hence stellar mass estimates. Our target galaxies have a range in stellar mass from 10^6 to $10^9 M_{\odot}$ with the majority of them in the mass range of 1 – $10 \times 10^7 M_{\odot}$. We note that in the stellar mass estimates by Perepelitsyna et al. (2014), the

galactic extinctions were not taken into account and an updated version of stellar masses by [Perepelitsyna et al. \(2014\)](#) is now available¹. We used the stellar mass estimates provided in the updated version. Our aim is to estimate and compare the instantaneous SFR of interacting and isolated dwarf galaxies in the sample. Young and massive OB-type stars emit significant amounts of radiation in the UV band. Imaging in UV will help to locate these populations and is therefore ideal for studying the star formation properties of galaxies. Of the 64 dwarf galaxies in our sample with stellar mass estimates, 58 are observed in the FUV ($\lambda_{\text{eff}} = 1538.6 \text{ \AA}$) band using the NASA GALEX mission ([Martin et al. 2005](#)). The GALEX FUV channel imaging is at a spatial resolution of $\sim 4.2''$ ([Morrissey et al. 2007](#)). The archival calibrated science-ready GALEX images of sample galaxies are obtained from the MAST data archive and are used for our further analysis. If a sample galaxy has multiple GALEX FUV channel observations, then we take the image corresponding to the highest exposure time, with exposure times ranging between $\sim 100 \text{ s}$ and $\sim 3300 \text{ s}$.

The basic parameters (taken from [Pustilnik & Tepliakova 2011](#); [Perepelitsyna et al. 2014](#); [Pustilnik & Martin 2016](#)) of the final sample of 58 galaxies are given in Table 1. The distance to each galaxy is taken from [Perepelitsyna et al. \(2014\)](#). These latter authors estimated the distance using the relation $D(\text{Mpc}) = V_{\text{dist}}/73(\text{km s}^{-1} \text{Mpc}^{-1})$, where V_{dist} is the velocity corresponding to the distance and taken from [Pustilnik & Tepliakova \(2011\)](#). For galaxies with reliable distances derived with photometric methods using Cepheids or stars from the tip of the red giant branch (TRGB), or with the surface-brightness fluctuation (SBF) method, [Pustilnik & Tepliakova \(2011\)](#) computed $V_{\text{dist}} = 73 (\text{km s}^{-1} \text{Mpc}^{-1}) \times D(\text{Mpc})$. For galaxies for which only redshifts were available, the contribution from the large negative peculiar velocity in the region considered was corrected while estimating V_{dist} . The uncertainty in the distance estimates is in the range of $0.4\text{--}0.6 \text{ Mpc}$. Of the final 58 galaxies, 22 are in pairs and/or have signatures of interaction. The integrated HI masses of most of the sample galaxies given in [Perepelitsyna et al. \(2014\)](#) and [Pustilnik & Martin \(2016\)](#) were measured using the Nançay Radio Telescope (NRT). For some galaxies, the measurements are taken from previous literature, such as [Pustilnik & Martin \(2016\)](#). The gas fraction given in Table 1 is the ratio of the total gas mass to the total baryonic mass, where the total gas mass is 1.33 times the HI mass (0.33 times the HI mass is taken as the Helium fraction) and the total baryonic mass is the sum of stellar mass and total gas mass ([Perepelitsyna et al. 2014](#)). The gas fraction of these galaxies suggests that they are gas-rich, with median values of 0.92 and 0.88 for interacting and isolated systems, respectively.

3. Analysis

As most of the FUV photons that emerge from a galaxy originate from the atmospheres of young stars ($\sim 100 \text{ Myr}$), the current SFR of a galaxy is proportional to the FUV luminosity emitted by the young stars. Under the assumption that the SFR is approximately constant over the past 100 Myr, the observed FUV flux from star forming galaxies is a direct tracer of current star formation ([Kennicutt 1998](#)). We used the following equation (Eq. (1)), as given in [Murphy et al. \(2011\)](#) for the GALEX FUV band, to estimate the current SFR of our sample of galaxies.

$$SFR_{\text{FUV}}[M_{\odot} \text{ yr}^{-1}] = 4.42 \times 10^{-44} L_{\text{FUV}}[\text{erg s}^{-1}] \dots \dots \quad (1)$$

¹ <https://arxiv.org/pdf/1408.0613.pdf>

[Murphy et al. \(2011\)](#) derived this formula from Starburst99 ([Leitherer et al. 1999](#)), assuming solar metallicity, and a Kroupa ([Kroupa 2001](#)) IMF, with a slope of -1.3 and -2.3 for stellar masses in the ranges of $0.1\text{--}0.5 M_{\odot}$ and $0.5\text{--}100 M_{\odot}$, respectively. We note that the calibration constant used in the relation can vary by up to a factor of ~ 1.5 with stellar metallicity (at lower metallicities the UV luminosity increases; [Bicker 2005](#)). We do not have metallicity information for all of the galaxies in our sample. The gas-phase metallicity values reported by [Perepelitsyna et al. \(2014\)](#) for some of them are lower than solar, but are approximately similar to each other in the same stellar mass range. Therefore, our final results based on the comparison of the SFR between the interacting and isolated galaxies in the same stellar mass range as our sample is not expected to be significantly affected by the choice of calibration constant.

We further analysed the calibrated GALEX images containing our sample galaxies in order to obtain the integrated FUV flux and L_{FUV} . From the $1^{\circ}5$ field of the GALEX tile, the region containing the sample galaxy is extracted. The extracted image has the sample galaxy at the centre and has dimensions equal to three times the Holmberg radius (corresponding to the B -band surface brightness level of $26.5 \text{ mag arcsec}^{-2}$) measured by [Perepelitsyna et al. \(2014\)](#) from optical images.

We identified the largest structure corresponding to the sample galaxy using the `astrodendro`² Python package. `Astrodendro` identifies structures in an intensity map for a given value of threshold flux, and a minimum number of pixels. We used three times the median value of the sky background as the threshold flux. The sky background is estimated using the sky background image corresponding to the target field provided in the GALEX MAST archive. The minimum number of pixels is taken as ten, which means that the structures that cover less than 10 pixels are not considered. This value is chosen because the area covered by 10 pixels is equivalent to a circle of ~ 1.8 pixels in radius, and therefore the size of the identified structure (~ 3.6 pixels) is comparable to or larger than the PSF of the observed field. The output of `astrodendro` provides the position, area, and flux of all the identified structures in a field. The largest structure (out of all the identified structures in a galaxy, the one with the maximum value for the area) corresponds to the entire galaxy and is identified. The top and bottom-left panels of Fig. 1 show the `astrodendro`-identified largest structures (in red) corresponding to some of the target galaxies in the GALEX FUV images. The top-left panel shows the galaxy DDO68, which is classified as interacting based on the irregular morphology identified in the HI maps as well as optical images ([Ekta 2008](#); [Annibali et al. 2016](#)). The top-right panel shows an isolated galaxy, UGC 5427. The bottom-left panel displays an interacting system, UGC 5272 and UGC 5272b, which has a HI bridge connecting the two galaxies ([Swaters et al. 2002](#)). The UGC 5272 is in the centre and UGC 5272b is $\sim 2 \text{ arcmin}$ towards the south. The bottom-right panel shows the subclumps (in dark blue) identified inside the UGC 5272–UGC 5272b system.

The flux of the largest structure, provided as an output by `astrodendro`, is taken as the total flux of the galaxy. To correct for the background, we used the sky background image corresponding to the target field taken from the GALEX MAST archive. The background corresponding to the galaxy is estimated by multiplying the exact area of the structure (provided by the `astrodendro` package) by the median background value and subtracted from the total flux. The measured integrated FUV flux is corrected for the Galactic foreground extinction using the values

² <https://dendrograms.readthedocs.io/en/stable/>

Table 1. Basic parameters of the sample galaxies.

Sl.no	Name or prefix	RA hh:mm:ss	Dec dd:mm:ss	Distance (Mpc)	Holmberg radius (")	Stellar mass ($\times 10^7 M_{\odot}$)	HI mass ($\times 10^7 M_{\odot}$)	Gas fraction	Remarks
1	SDSS	07 23 01.420	+36 21 17.100	16.0	39.2	2.76	22.60	0.92	Pair of 2
2	SDSS	07 23 13.460	+36 22 13.000	16.0	9.1	0.07	9.61	0.99	Pair of 1
3	MCG9-13-52	07 46 56.360	+51 17 42.800	10.1	32.3	1.32	6.25	0.86	Pair of 4
4	MCG9-13-56	07 47 32.100	+51 11 29.000	10.0	32.8	2.46	13.69	0.88	Pair of 3
5	NGC2541	08 14 40.180	+49 03 42.100	12.0	186.7	95.03	460.82	0.87	Pair of 6
6	NGC 2552	08 19 20.140	+50 00 25.200	11.11	123.2	41.66	83.01	0.73	Pair of 5
7	HS 0822+3542	08 25 55.430	+35 32 31.900	13.49	9.7	0.04	1.46	0.98	Pair of 8
8	SAO0822+3545	08 26 05.590	+35 35 25.700	13.49	15.1	0.16	4.30	0.97	Pair of 7
9	SDSS	08 52 33.750	+13 50 28.300	23.08	20.6	2.98	26.40	0.92	Pair of 10
10	SDSS	08 52 40.940	+13 51 56.900	23.08	6.4	0.22	–	–	Pair of 9
11	UGC4704	08 59 00.280	+39 12 35.700	11.74	200.5	6.73	72.86	0.94	Pair of 12
12	SDSS	08 59 46.930	+39 23 05.600	11.63	19.5	0.96	1.56	0.69	Pair of 11
13	UGC4722	09 00 23.540	+25 36 40.600	27.89	122.8	22.59	212.9	0.93	Merger
14	KUG0934+277	09 37 47.650	+27 33 57.700	25.16	29.6	7.35	45.42	0.89	Pair
15	UGC5272b	09 50 19.490	+31 27 22.300	10.27	15.8	0.19	2.89	0.95	Pair of 16
16	UGC5272	09 50 22.400	+31 29 16.000	10.3	86.2	3.41	46.33	0.95	Pair of 15
17	UGC5540	10 16 21.700	+37 46 48.700	19.16	81.1	26.89	46.55	0.70	Pair of 18
18	HS 1013+3809	10 16 24.500	+37 54 46.000	19.3	18.1	0.33	13.28	0.98	Pair of 17
19	UGC3672	07 06 27.560	+30 19 19.400	16.93	47.0	2.6	79.50	0.98	Part of a triplet
20	UGC3860	07 28 17.200	+40 46 13.000	7.81	56.1	2.13	16.92	0.91	Tidal features
21	UGC4117	07 57 25.980	+35 56 21.000	14.12	41.6	3.57	23.73	0.90	Tidal features
22	DD068	09 56 45.700	+28 49 35.000	9.86	80.7	1.5	66.35	0.98	Tidal features
23	UGC3600	06 55 40.000	+39 05 42.800	9.3	74.4	1.91	11.23	0.89	Isolated
24	SDSS	07 30 58.900	+41 09 59.800	15.7	21.3	2.36	4.36	0.71	Isolated
25	SDSS	07 37 28.470	+47 24 32.800	10.42	19.6	0.11	2.51	0.97	Isolated
26	UGC3966	07 41 26.000	+40 06 44.000	8.64	52.3	1.22	44.26	0.98	Isolated
27	SDSS	07 44 43.720	+25 08 26.600	12.95	10.0	0.3	1.38	0.86	Isolated
28	UGC4148	08 00 23.680	+42 11 37.000	13.55	65.6	2.95	54.15	0.98	Isolated
29	NGC2500	08 01 53.300	+50 44 15.400	10.88	117.0	126.82	96.60	0.50	Isolated
30	MCG7-17-19	08 09 36.100	+41 35 40.000	13.37	44.8	5.74	25.31	0.85	Isolated
31	SDSS	08 10 30.650	+18 37 04.100	23.05	15.5	1.15	6.27	0.88	Isolated
32	SDSS	08 12 39.530	+48 36 45.400	11.05	20.0	0.37	4.85	0.95	Isolated
33	NGC2537	08 13 14.730	+45 59 26.300	9.86	78.1	120.2	48.44	0.35	Isolated
34	IC2233	08 13 58.930	+45 44 34.300	10.7	380.5	25.25	54.30	0.74	Isolated
35	UGC4426	08 28 28.530	+41 51 22.800	10.3	69.4	6.18	27.05	0.85	Isolated
36	SDSS	08 31 41.210	+41 04 53.700	11.64	13.0	0.59	0.58	0.57	Isolated
37	SDSS	08 43 37.980	+40 25 47.200	12.05	12.9	0.41	0.62	0.67	Isolated
38	SDSS	09 11 59.430	+31 35 35.900	13.52	9.1	0.24	1.81	0.91	Isolated
39	IC2450	09 17 05.270	+25 25 44.900	25.47	62.6	185.06	12.4	0.08	Isolated
40	SDSS	09 26 09.450	+33 43 04.100	10.63	47.9	0.13	6.77	0.99	Isolated
41	SDSS	09 28 59.060	+28 45 28.500	19.9	24.7	8.32	23.37	0.79	Isolated
42	SDSS	09 29 51.830	+11 55 35.700	24.29	31.4	2.76	45.94	0.96	Isolated
43	SDSS	09 31 36.150	+27 17 46.600	23.6	18.2	1.06	7.09	0.90	Isolated
44	SDSS	09 40 03.270	+44 59 31.700	20.71	10.7	1.6	1.1	0.7	Isolated
45	KISSB23	09 40 12.670	+29 35 29.300	10.21	36.4	1.29	5.41	0.85	Isolated
46	UGC5186	09 42 59.100	+33 16 00.200	10.77	50.2	2.08	2.57	0.62	Isolated
47	SDSS	09 43 42.970	+41 34 08.900	22.77	16.3	2.47	4.89	0.73	Isolated
48	SDSS	09 44 37.110	+10 00 46.300	22.22	24.3	3.88	25.98	0.90	Isolated
49	UGC5209	09 45 04.200	+32 14 18.200	10.55	29.8	1.87	4.02	0.74	Isolated
50	SDSS	09 47 18.350	+41 38 16.400	22.56	12.9	0.46	1.2	0.78	Isolated
51	SDSS	09 47 58.450	+39 05 10.100	25.21	15.9	17.66	104.99	0.89	Isolated
52	SDSS	09 51 41.670	+38 42 07.300	23.07	16.7	1.77	6.02	0.82	Isolated
53	SDSS	09 54 50.600	+36 20 01.900	10.22	14.8	0.16	0.62	0.84	Isolated
54	PC0956+4751	09 59 18.600	+47 36 58.400	18.66	29.0	1.91	14.87	0.91	Isolated
55	KUG0959+299	10 02 23.180	+29 43 33.300	13.48	14.8	0.58	–	–	Isolated
56	UGC5427	10 04 41.050	+29 21 55.200	9.79	49.9	5.2	5.98	0.60	Isolated
57	UGC 5464	10 08 07.700	+29 32 34.400	16.9	54.8	9.58	19.29	0.73	Isolated
58	SDSS	10 10 14.960	+46 17 44.100	18.58	12.9	0.57	0.49	0.53	Isolated

Notes. Parameters are taken from Pustilnik & Tepliakova (2011), Perepelitsyna et al. (2014), and Pustilnik & Martin (2016). The first 22 galaxies are those that are interacting.

provided by Schlegel et al. (1998) and applying the calibration given by Schlafly & Finkbeiner (2011; R_{FUV} is taken as 8.06 from Bianchi 2011). The extinction-corrected integrated UV flux is converted to L_{FUV} using the distance values given in Table 1. Using the estimated L_{FUV} and the SFR formula given in Eq. (1), we estimated the SFR of each galaxy. The estimated total luminosity and SFR of each galaxy are tabulated in Table 2. We did

not correct for the internal extinction and also the R_{FUV} values for low-mass galaxies can be different (generally seems to be up to ~ 1.5 times higher, Bianchi 2011) from the assumed value based on the Milky Way. The estimated FUV flux or luminosity is therefore a lower limit, as is the derived SFR. Using astrodendro, we also identified the star forming clumps (the smallest structure appearing in the GALEX image, which cannot be split

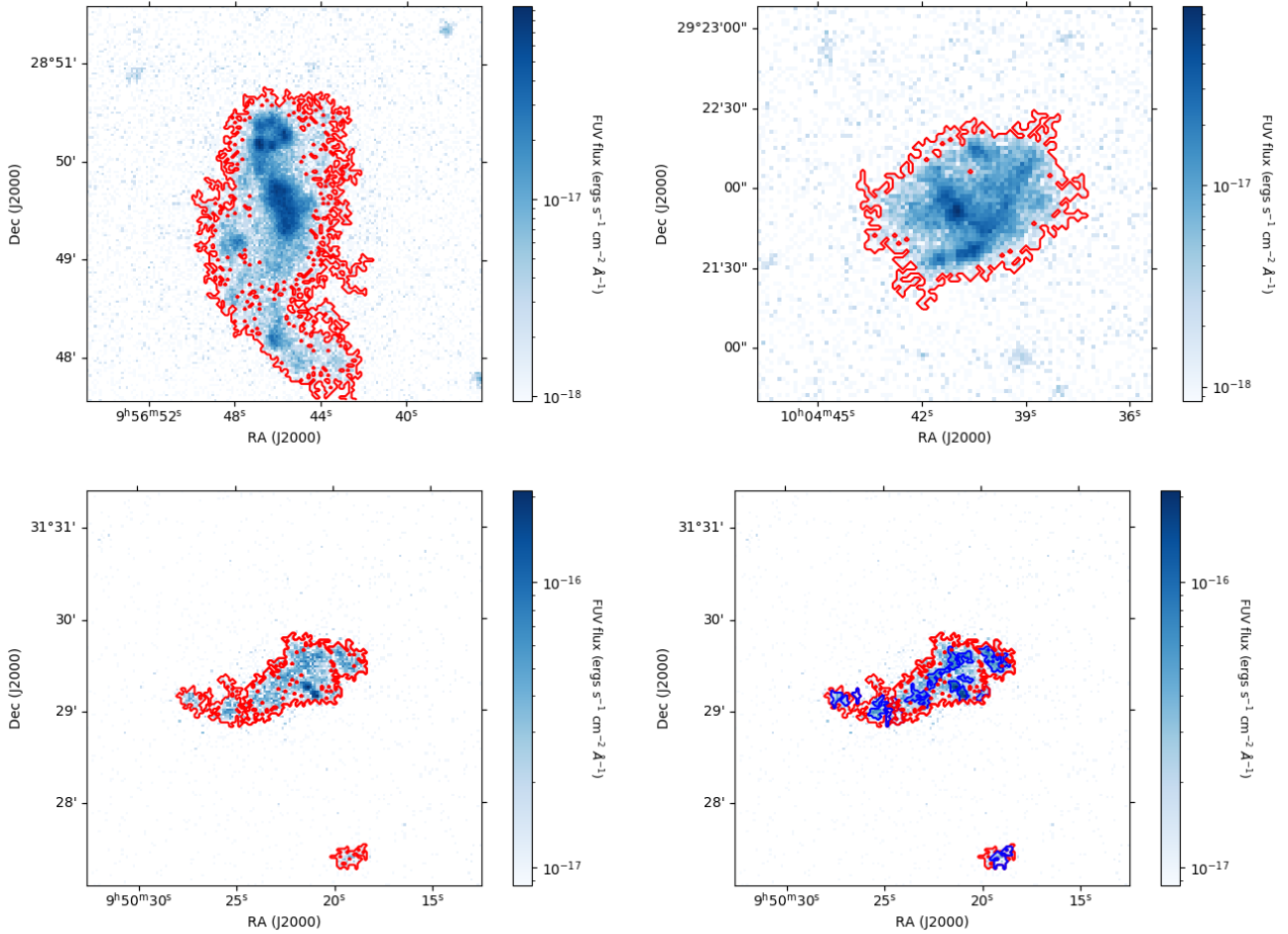


Fig. 1. Astrodendro-identified largest structures corresponding to some of the target galaxies in the GALEX FUV images. The top-left, top-right, and bottom-left panels show the largest structures (in red) corresponding to the galaxies DDO 68 (a galaxy classified as interacting based on the presence of tidal features), UGC 5427 (an isolated single dwarf), and the UGC 5272/5272b interacting system, respectively. In the bottom-left panel, the UGC 5272 is in the centre and UGC 5272b is ~ 2 arcmin towards the south. The bottom-right panel shows the subclumps (in dark blue) identified inside the UGC 5272/5272b system.

further) in these galaxies. The number of clumps identified, their sizes, and their star formation rate density (SFRD) are listed in Table 2. As the galaxies of our sample are intrinsically smaller in size, and also given the poor spatial resolution of GALEX, there are not many clumps identified in most of the sample galaxies. The structure corresponding to the entire galaxy is the only structure identified in most of the galaxies and their sizes are comparable to the optical size of these galaxies, given in Table 2 of [Perpelitsyna et al. \(2014\)](#). The clumps identified in GALEX images can actually be composed of multiple smaller clumps, which we were not able to resolve due to the limited angular resolution. Therefore, the size of individual star-forming clumps would be smaller than the values noted in Table 2. Deeper and higher-spatial-resolution UV observations (e.g. using the Ultraviolet Imaging Telescope, UVIT, on board AstroSat) are required in order to identify smaller star forming clumps, study their spatial distribution, and carry out any meaningful analysis of the SFRD values of the star forming clumps.

4. Results and discussion

To understand the effect of interactions on the SFR, we analysed the correlation between the derived instantaneous SFR and the stellar mass of the galaxies in our sample. To this end, we plot-

ted the derived instantaneous SFR of our sample against stellar mass (left panel of Fig. 2). The stars and circles represent the interacting and isolated set of galaxies, respectively. The errors in the derived SFR are of the order of 10^{-2} dex and the error bars are shorter than the size of the points and are therefore not shown. The figure shows that the SFR increases as stellar mass increases, for both the interacting and isolated galaxies. When we consider the location of the interacting systems in galaxy scaling relations to check for correlations or offsets, it is essential to understand whether the parameters are estimated for the entire system or for individual components. As described in Sect. 2, there are 22 interacting galaxies in our sample and these are in different stages of interaction. There are 16 (8×2) galaxies are in pairs where both galaxies are well separated in optical/UV images but show a common envelope around them in HI and/or are at similar distances with perturbed morphology, indicating that they are pair. The current SFR of each galaxy in these eight pairs ($8 \times 2 = 16$ galaxies) is calculated separately and these values are plotted against their respective stellar mass. Six single galaxies that show tidal tails and a perturbed morphology in the HI maps and/or optical images are also considered as interacting galaxies in our study. The perturbed morphology of these six single galaxies, which are classified as interacting systems, could be the effect of a past fly-by event, with tidal

Table 2. Derived FUV luminosity and SFR of sample galaxies.

Sl.no	L_{FUV} $\times 10^{39} \text{ erg s}^{-1}$	SFR $\times 10^{-4} (M_{\odot} \text{ yr}^{-1})$	No of clumps	Size of clumps (pc)	SFRD of clumps ($\times 10^{-4} (M_{\odot} \text{ yr}^{-1} \text{ kpc}^{-2})$)
1	18.76 ± 0.20	8.29 ± 0.09	4	227.35–359.47 (284.47)	6.36–8.85 (7.41)
2	4.15 ± 0.07	1.83 ± 0.03	1	334.65	5.22
3	12.02 ± 0.20	5.31 ± 0.09	5	143.51–198.69 (175.77)	9.74–12.55 (10.57)
4	141.50 ± 1.08	62.54 ± 0.48	4	147.89–246.11 (188.61)	12.93–98.76 (65.53)
5	1378.40 ± 0.62	609.25 ± 0.27	198	155.65–767.30 (225.57)	0.78–34.68 (2.26)
6	518.54 ± 0.49	229.19 ± 0.22	89	144.11–407.61 (203.80)	1.00–23.55 (3.47)
7	19.38 ± 0.06	8.57 ± 0.03	1	479.21	11.88
8	13.78 ± 0.05	6.09 ± 0.02	1	727.81	3.66
9	30.27 ± 0.18	13.38 ± 0.08	4	366.66–912.97 (401.50)	1.44–3.52 (1.93)
10	3.44 ± 0.04	1.52 ± 0.02	1	491.92	2.00
11	135.30 ± 0.26	59.80 ± 0.12	21	152.28–502.76 (198.55)	0.59–15.70 (3.05)
12	8.68 ± 0.04	3.83 ± 0.02	2	297.92–518.21 (408.06)	0.98–3.91 (2.45)
13	840.09 ± 5.12	371.32 ± 2.26	5	594.44–816.99 (667.07)	19.57–37.63 (22.33)
14	76.52 ± 1.06	33.82 ± 0.47	3	326.36–765.37 (565.27)	6.47–10.25 (10.04)
15	7.72 ± 0.11	3.41 ± 0.05	2	151.89–230.73 (191.31)	7.64–9.20 (8.42)
16	226.60 ± 1.22	100.16 ± 0.54	21	133.60–307.58 (174.20)	6.26–55.43 (18.56)
17	199.73 ± 2.86	88.28 ± 1.26	5	248.53–745.59 (324.04)	15.97–41.22 (23.04)
18	221.80 ± 2.92	98.04 ± 1.29	1	755.19	54.74
19	107.78 ± 0.79	47.64 ± 0.35	2	568.43–839.10 (703.76)	10.90–16.07 (13.49)
20	40.08 ± 0.06	17.72 ± 0.03	18	101.31–256.28 (143.27)	1.64–10.20 (4.99)
21	100.91 ± 1.24	44.60 ± 0.55	9	183.15–474.08 (216.71)	9.73–21.92 (13.66)
22	203.75 ± 0.27	90.06 ± 0.12	42	127.90–561.87 (171.59)	0.47–30.88 (1.69)
23	23.55 ± 0.13	10.41 ± 0.06	12	126.52–497.38 (147.66)	3.37–6.53 (4.89)
24	40.18 ± 0.18	17.76 ± 0.08	1	737.08	10.41
25	3.53 ± 0.05	1.56 ± 0.02	1	237.97	8.77
26	64.99 ± 0.07	28.73 ± 0.03	26	117.54–506.19 (166.23)	1.14–8.22 (2.67)
27	5.67 ± 0.10	2.51 ± 0.04	1	314.26	8.09
28	84.73 ± 0.16	37.45 ± 0.07	8	200.40–707.42 (294.06)	2.18–8.40 (3.89)
29	1009.28 ± 0.54	446.10 ± 0.24	94	141.13–518.53 (194.53)	0.90–48.23 (4.67)
30	113.45 ± 0.81	50.15 ± 0.36	4	189.98–567.29 (266.09)	6.17–31.65 (20.68)
31	13.45 ± 0.06	5.94 ± 0.03	1	940.74	2.14
32	10.17 ± 0.02	4.50 ± 0.01	1	623.12	3.69
33	552.33 ± 0.30	244.13 ± 0.13	30	127.90–299.94 (171.59)	1.26–151.13 (2.09)
34	410.49 ± 0.40	181.43 ± 0.18	28	138.79–496.56 (180.65)	0.98–39.88 (11.82)
35	31.71 ± 0.07	14.02 ± 0.03	35	133.60–387.22 (202.62)	0.86–5.07 (1.49)
36	4.80 ± 0.07	2.12 ± 0.03	1	301.97	7.41
37	8.56 ± 0.18	3.78 ± 0.08	1	283.94	14.95
38	13.18 ± 0.03	5.83 ± 0.01	1	594.71	5.25
39	281.19 ± 2.67	124.29 ± 1.18	1	1325.63	22.52
40	13.16 ± 0.23	5.82 ± 0.10	6	157.21–242.77 (182.38)	6.08–9.89 (7.58)
41	29.74 ± 0.47	13.14 ± 0.21	1	642.73	10.13
42	40.32 ± 0.67	17.82 ± 0.30	4	330.45–668.37 (404.67)	4.08–6.67 (4.90)
43	15.11 ± 0.32	6.68 ± 0.14	2	349.03–421.96 (385.50)	4.90–7.70 (6.30)
44	6.30 ± 0.25	2.78 ± 0.11	1	306.29	9.45
45	43.88 ± 0.40	19.39 ± 0.18	1	539.59	21.21
46	12.18 ± 0.28	5.38 ± 0.12	1	366.96	12.73
47	21.30 ± 0.64	9.42 ± 0.28	2	336.76–407.12 (371.94)	9.29–10.74 (10.01)
48	51.83 ± 0.14	22.91 ± 0.06	8	302.29–455.72 (369.84)	1.40–4.66 (3.04)
49	10.71 ± 0.15	4.74 ± 0.07	3	173.10–348.89 (202.98)	5.25–7.74 (6.25)
50	23.23 ± 0.67	10.27 ± 0.30	1	471.85	14.69
51	6.53 ± 0.30	2.89 ± 0.13	1	342.97	7.82
52	8.64 ± 0.34	3.82 ± 0.15	1	313.85	12.34
53	2.11 ± 0.08	0.93 ± 0.03	1	192.11	8.07
54	16.53 ± 0.46	7.31 ± 0.20	3	242.04–342.30 (242.04)	7.27–11.85 (8.75)
55	10.48 ± 0.17	4.63 ± 0.08	1	435.38	7.78
56	68.51 ± 0.13	30.28 ± 0.06	12	133.19–295.09 (160.63)	0.53–17.64 (8.68)
57	30.58 ± 0.59	13.52 ± 0.26	5	229.91–373.31 (285.82)	8.64–12.22 (9.58)
58	16.15 ± 0.29	7.14 ± 0.13	1	488.00	9.55

Notes. The number and properties of the star forming clumps identified in each galaxy are also given, with their median properties given in parentheses.

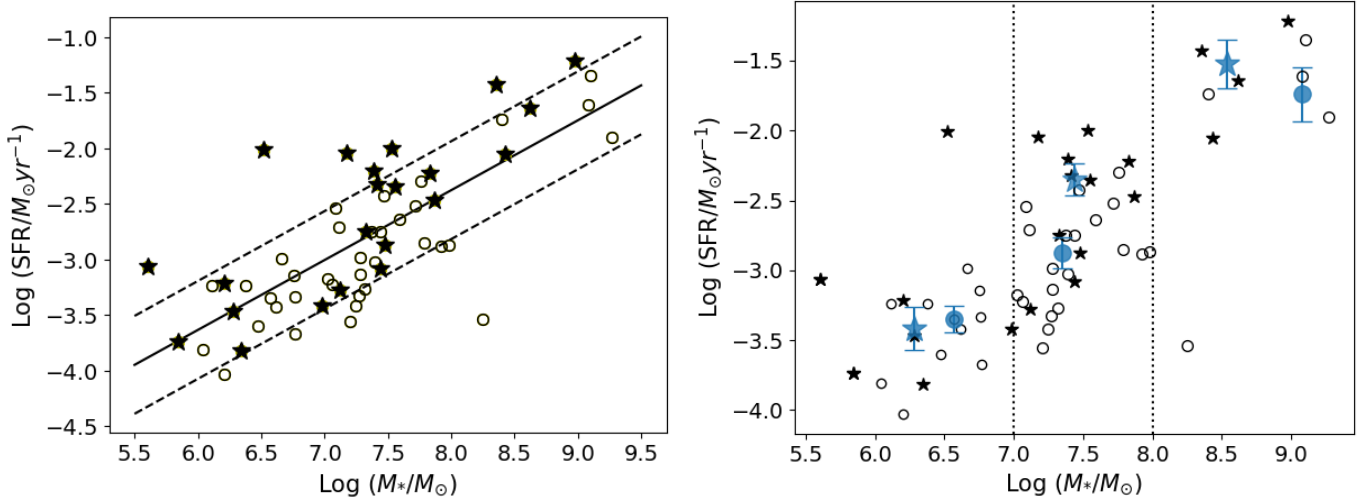


Fig. 2. Instantaneous SFR vs. M_* for our sample galaxies. The black stars and open circles in both panels represent the interacting and isolated dwarf galaxies, respectively. Left panel: solid and dotted lines represent the best-fit line and the \pm rms lines, respectively. Right panel: dotted lines show the mass bin of $10^{7-8} M_\odot$. The blue solid star and closed circle correspond to the median $\log(\text{SFR})$ values of the sample in different mass bins.

features, or may indicate that the galaxy is a merger remnant with multiple smaller systems together. For these galaxies, the SFR is calculated based on the FUV flux of the entire system. Similarly, the stellar mass of these galaxies taken from the study of [Perepelitsyna et al. \(2014\)](#) is calculated using the integrated colour and luminosity of the entire system from SDSS images. Specifically, these latter authors used the g -band luminosity and $(g-i)$ colour relations provided by [Zibetti et al. \(2009\)](#), because this combination yields the most robust estimates in the optical part of the spectrum and the mass- g -band luminosity ratio takes into account the complex star formation history observed in low-mass galaxies including the recent episodes of star formation. Considering all these points, we expect these systems to follow the expected correlation between the current SFR (estimated from FUV luminosity) and stellar mass (estimated using the g -band luminosity and $(g-i)$ colour relation). Any deviation from the expected SFR corresponding to a stellar mass could be due to a real increase or decrease in star formation. This assumption is valid even when the current SFR and the stellar estimates are dominated by that of the main galaxy of the system, and some outer regions corresponding to tidal tails or accreted systems are not considered (because of their low surface brightness). However, this assumption will not be valid if the current SFR is concentrated only in some regions of the galaxies (which might be the tidal tails or accreted systems) and we compare it against the total stellar mass of the system, which might be dominated by the main galaxy. Based on the analysis presented here, we see that the star formation identified in all the galaxies of our sample (including these six galaxies classified as interacting based on their perturbed morphology) is widespread over the entire system and is not concentrated to any specific regions. We therefore expect these galaxies to follow the stellar mass-SFR scaling relation and any deviation from this relation can be considered as real. We therefore performed a linear fit to the entire sample. A positive correlation between the $\log(\text{SFR})$ and $\log(\text{stellar mass})$ is found, with a slope of 0.62 and an intercept of -7.4 . The best-fit line is shown as a solid black line in the figure. The rms scatter in $\log(\text{SFR})$ is 0.44 dex and the dotted lines correspond to ± 0.44 dex to the best-fit $\log(\text{SFR})$. Most of the points are within the \pm rms scatter. However, the majority of the galaxies in the

interacting sample are above the best-fit line (with six galaxies above the $+$ rms scatter line) and the majority of the galaxies in the isolated sample are below the best-fit line.

There is an insufficient number of interacting and isolated galaxies in the entire mass range to separately fit the two sets. Most of the galaxies in our sample (31/58, with 11 interacting and 20 isolated galaxies) are in the mass range of $10^7-10^8 M_\odot$. We selected this mass bin (as shown by two vertical dotted lines in the right panel of Fig. 2) and estimated the median $\log(\text{SFR})$ of the interacting and isolated sample. The median SFR is 3.4 ± 1.2 times higher for the interacting sample than that of the isolated sample in this mass bin. The median values are shown as a transparent purple star and circle for the interacting and isolated samples, respectively. The remaining mass bins are not equally populated with the two sets. We therefore estimated the median $\log(\text{SFR})$ of the interacting and isolated sample with stellar mass $<10^7 M_\odot$ and $>10^8 M_\odot$ and shown in the right panel of Fig. 2. The ratio of the median SFR of the interacting sample to that of the isolated sample in the mass bins with stellar mass $<10^7 M_\odot$ and stellar mass $>10^8 M_\odot$ is ~ 0.85 and 1.65, respectively. Both these mass bins contain fewer galaxies compared to the middle mass bin. The galaxies of the sample in the lower mass bin (stellar mass $<10^7 M_\odot$) have $M_B > -13.5$ mag and therefore this mass bin could be significantly affected by the incompleteness of the initial sample as described in Sect. 2. There is a slight enhancement of SFR for the interacting sample compared to the isolated sample in the higher mass bin (stellar mass $>10^8 M_\odot$). We note that the stage and nature of the interaction (major or minor merger, non-merger interactions, and the projected distance between the pair) can also affect the SFR. However, the number of galaxies in our current sample is not sufficient to make a statistical and meaningful comparison between the subclasses based on these parameters.

Most of the previous observational studies of low-mass galaxies exploring the effect of interactions on their evolution were focused on individual systems. The first systematic study to understand environmental effects on star formation using a large sample of dwarf galaxy pairs was performed by [Stierwalt et al. \(2015\)](#). Their sample covered a mass range of $10^7-5 \times 10^9 M_\odot$ and a redshift range of $0.005 < z < 0.07$. Based on the presence

or absence of a massive galaxy (stellar mass $>5 \times 10^9 M_{\odot}$) at a distance <1.5 Mpc, these pairs were again classified as non-isolated or isolated pairs. The median mass of the sample was $10^{8.9} M_{\odot}$. More than 90% of the pairs in the sample had a mass ratio of <5 . These latter authors observed an enhancement in the SFR of the dwarf galaxies in pairs by a factor of $2.3 (\pm 0.7)$ compared to that of the isolated single dwarfs (matched in redshift and stellar mass), for pair separations of <50 kpc. Such an enhancement was observed for both isolated and non-isolated pairs. This suggests that close encounters between dwarf galaxies do enhance their SFR, irrespective of the presence or absence of a massive neighbour. Stierwalt et al. (2015) also found that the enhancement decreases with increasing pair separation and was observed out to pair separations as far as 100 kpc for isolated dwarf pairs. The enhancement in SFR for dwarf pairs, by a factor of $2.3 (\pm 0.7)$, observed by these latter authors is comparable to the enhancement factor of 3.4 ± 1.2 observed in the present study. We note that the sample in our study is smaller and cannot therefore be subclassified based on pair separation distance and mass ratio as in the study by Stierwalt et al. (2015). Also, the median stellar mass of our sample is $\sim 2.3 \times 10^7 M_{\odot}$, whereas that of the sample in the study of Stierwalt et al. (2015) is $10^{8.9} M_{\odot}$.

Knapen et al. (2015) studied a sample of approximately 1500 of the nearest galaxies (with stellar masses in the range $10^{8.0-11.0} M_{\odot}$) – all within a distance of ~ 45 Mpc – to investigate the influence of interactions on star formation. This representative sample of nearby galaxies includes many low-mass galaxies (stellar mass $<10^9 M_{\odot}$, but with most of them in the range $10^{8.0-9.0} M_{\odot}$). These authors found that both SFR and sSFR (which is SFR normalised by the stellar mass of the galaxy) are enhanced in interacting galaxies. The increase is moderate, reaching a maximum of a factor of 1.9 for the highest degree of interaction (mergers). A recent study by Sun et al. (2020) explored the environmental influence on star formation in low-mass galaxies using the SDSS-IV/MaNGA spatially and spectroscopically resolved data of 386 low-mass galaxies with stellar mass in the range $10^{8-10} M_{\odot}$ (with median stellar mass of $\sim 10^{9.5} M_{\odot}$) and at redshifts of $0.01 < z < 0.07$. These authors found that star formation activities in low-mass galaxies are affected by their environment and found an enhancement in their SFR. For the pair candidates with mass ratios of between 0.25 and 4 and at projected distances of <100 kpc, they found an enhancement in SFR by a factor of 1.75 ± 0.96 in the inner regions, with this enhancement factor decreasing outwards. Though the properties of the sample (such as stellar mass and distance) in these previous studies are different from those presented in our study, the observed factors of enhancement in the SFR of interacting dwarfs compared to isolated dwarfs in these studies are comparable to the values we find for our sample.

Recently, Martin et al. (2021) used simulations of low-mass galaxies to investigate the effect of mergers and interactions on their star formation, and their evolution up to a redshift of 0.5. These authors found that the mergers drive a moderate enhancement in star formation (3–4 times at $z = 1$) and non-merger interactions drive a smaller enhancement in star formation (~ 2 times). However, non-merger interactions are numerous compared to major and minor mergers and therefore contribute to the stellar mass growth of dwarf galaxies. Figure 9 of this latter publication shows the average displacement of galaxies in their simulation from the best-fit star forming main sequence in the $\log(\text{SFR})$ versus stellar mass plot. This plot shows that the galaxies in the mass range $10^{7.5-9} M_{\odot}$ have a displacement of 0.45–0.85 dex at the redshift of $z = 0.5$. The highest displace-

ment is for those galaxies that undergo major mergers and the lowest is for those that undergo non-merger interactions. The rms scatter we measure in $\log(\text{SFR})$ based on the left panel of Fig. 2 is 0.44 dex and the enhancement in SFR for the interacting systems compared to the isolated system in the mass bin of $10^{7.0-8} M_{\odot}$ is 3.35. As the redshift and nature of interaction in our sample are different, we cannot directly compare our observed results with those obtained from these latter simulations. Our sample contains galaxies that are post-merger products, which undergo minor mergers and non-merger interactions and have a range of projected separation. However, it is still interesting to see that our observed values are comparable with the simulation results, suggesting a role of interactions in the enhancement of SFR in our sample. We note that the SFR used in the $\log(\text{SFR})$ versus stellar-mass plot (Fig. 2) and in Fig. 8 of Martin et al. (2021) is the current or instantaneous SFR of the galaxies.

5. Summary

The effect of interactions on the evolution of low-mass galaxies is not well understood. In the present study, we performed a UV study of a sample of 22 interacting and 36 single gas-rich dwarf galaxies in the Lynx-Cancer void region using FUV images from the GALEX mission. We estimated their instantaneous SFR from their FUV luminosity in order to understand the effect of interactions on their SFR. We find an enhancement in SFR by a factor of 3.4 ± 1.2 for the interacting systems compared to single dwarf galaxies in the stellar mass range $10^7-10^8 M_{\odot}$. This value is comparable to the enhancement found by previous observational studies in the SFR of low-mass interacting galaxies, with stellar masses of $\sim 10^9 M_{\odot}$. Also similar to the predictions based on the simulation of dwarf galaxies, in the mass range of $10^{7.5-9} M_{\odot}$ at a redshift of ~ 0.5 . Our results suggest that the dwarf–dwarf galaxy interactions can lead to an enhancement in their SFR. Although our sample contains fewer galaxies, this study provides the first quantitative insights into the nature of interactions of dwarf galaxies in the sub- $10^8 M_{\odot}$ regime and increases the small number of interacting dwarfs in the local Universe studied in the FUV. In future, we plan to study a larger sample of dwarf galaxies in different stages of interactions (major and minor mergers, fly-bys, etc.) in order to understand the effect of these different stages in their SFR. Future deeper and higher-spatial-resolution UV studies will help to improve our understanding of the effect of dwarf-galaxy interactions on the spatial distribution of star forming clumps and will also help us to identify star formation in tidal tails.

Acknowledgements. We thank the referee for the insightful suggestions which have improved the manuscript significantly. S.S. acknowledges support from the Science and Engineering Research Board of India through Ramanujan Fellowship and POWER grant (SPG/2021/002672). This work used Astropy and Matplotlib software packages (Astropy Collaboration 2013, 2018, 2022; Hunter 2007).

References

- Annibali, F., Nipoti, C., Ciotti, L., et al. 2016, *ApJ*, 826, L27
- Annibali, F., Beccari, G., Bellazzini, M., et al. 2020, *MNRAS*, 491, 5101
- Aragon-Calvo, M. A., & Szalay, A. S. 2013, *MNRAS*, 428, 3409
- Astropy Collaboration (Robitaille, T. P., et al.) 2013, *A&A*, 558, A33
- Astropy Collaboration (Price-Whelan, A. M., et al.) 2018, *AJ*, 156, 123
- Astropy Collaboration (Price-Whelan, A. M., et al.) 2022, *ApJ*, 935, 167
- Barnes, J. E., & Hernquist, L. E. 1991, *ApJ*, 370, L65
- Barton, E. J., Geller, M. J., & Kenyon, S. J. 2000, *ApJ*, 530, 660
- Bellazzini, M., Oosterloo, T., Fraternali, F., & Beccari, G. 2013, *A&A*, 559, L11
- Bianchi, L. 2011, *Ap&SS*, 335, 51

- Bicker, J., & Fritze-v. Alvensleben, U., 2005, *A&A*, **443**, L19
- Bickley, R. W., Ellison, S. L., Patton, D. R., et al. 2022, *MNRAS*, **514**, 3294
- Brown, W., Patton, D. R., Ellison, S. L., & Faria, L. 2023, *MNRAS*, **522**, 5107
- Byrne-Mamahit, S., Hani, M. H., Ellison, S. L., Quai, S., & Patton, D. R. 2023, *MNRAS*, **519**, 4966
- Cao, C., Xu, C. K., Domingue, D., et al. 2016, *ApJS*, **222**, 16
- Carlin, J. L., Sand, D. J., Price, P., et al. 2016, *ApJ*, **828**, L5
- Chengalur, J. N., & Pustilnik, S. A. 2013, *MNRAS*, **428**, 1579
- Di Matteo, P., Combes, F., Melchior, A. L., & Semelin, B. 2007, *A&A*, **468**, 61
- D'Onghia, E., & Lake, G. 2008, *ApJ*, **686**, L61
- Du, W., Cheng, C., Zheng, Z., & Wu, H. 2020, *AJ*, **159**, 138
- Dubois, Y., Beckmann, R., Bournaud, F., et al. 2021, *A&A*, **651**, A109
- Ekta, Chengalur, J. N., & Pustilnik, S. A. 2008, *MNRAS*, **391**, 881
- Ellison, S. L., Patton, D. R., Simard, L., et al. 2010, *MNRAS*, **407**, 1514
- Fakhouri, O., Ma, C.-P., & Boylan-Kolchin, M. 2010, *MNRAS*, **406**, 2267
- Grazian, A., Fontana, A., Santini, P., et al. 2015, *A&A*, **575**, A96
- Hernquist, L. 1989, *Nature*, **340**, 687
- Higgs, C. R., & McConnachie, A. W. 2021, *MNRAS*, **506**, 2766
- Higgs, C. R., McConnachie, A. W., Irwin, M., et al. 2016, *MNRAS*, **458**, 1678
- Hopkins, P. F., Cox, T. J., Hernquist, L., et al. 2013, *MNRAS*, **430**, 1901
- Huertas-Company, M., Bernardi, M., Pérez-González, P. G., et al. 2016, *MNRAS*, **462**, 4495
- Hunter, J. D. 2007, *Comput. Sci. Eng.*, **9**, 90
- Izotov, Y. I., & Thuan, T. X. 2009, *ApJ*, **690**, 1797
- Kado-Fong, E., Greene, J. E., Greco, J. P., et al. 2020, *AJ*, **159**, 103
- Kennicutt, R. C., Jr. 1998, *ApJ*, **498**, 541
- Knapen, J. H., Cisternas, M., & Querejeta, M. 2015, *MNRAS*, **454**, 1742
- Koposov, S. E., Belokurov, V., Torrealba, G., & Evans, N. W. 2015, *ApJ*, **805**, 130
- Kroupa, P. 2001, *MNRAS*, **322**, 231
- Leitherer, C., Schaerer, D., Goldader, J. D., et al. 1999, *ApJS*, **123**, 3
- Lelli, F., Verheijen, M., & Fraternali, F. 2014, *MNRAS*, **445**, 1694
- Li, Y.-S., & Helmi, A. 2008, *MNRAS*, **385**, 1365
- Liu, C.-X., Pan, D. C., Hao, L., et al. 2015, *ApJ*, **810**, 165
- Martin, D. C., Fanson, J., Schiminovich, D., et al. 2005, *ApJ*, **619**, L1
- Martín, G., Jackson, R. A., Kaviraj, S., et al. 2021, *MNRAS*, **500**, 4937
- Martínez-Delgado, D., Romanowsky, A. J., Gabany, R. J., et al. 2012, *ApJ*, **748**, L24
- Mihos, J. C., & Hernquist, L. 1994a, *ApJ*, **425**, L13
- Mihos, J. C., & Hernquist, L. 1994b, *ApJ*, **431**, L9
- Mihos, J. C., & Hernquist, L. 1996, *ApJ*, **464**, 641
- Moreno, J., Torrey, P., Ellison, S. L., et al. 2019, *MNRAS*, **485**, 1320
- Morrissey, P., Conrow, T., Barlow, T. A., et al. 2007, *ApJS*, **173**, 682
- Murphy, E. J., Condon, J. J., Schinnerer, E., et al. 2011, *ApJ*, **737**, 67
- Padmanabhan, H., & Loeb, A. 2020, *MNRAS*, **496**, 1124
- Patton, D. R., Ellison, S. L., Simard, L., McConnachie, A. W., & Mendel, J. T. 2011, *MNRAS*, **412**, 591
- Patton, D. R., Torrey, P., Ellison, S. L., Mendel, J. T., & Scudder, J. M. 2013, *MNRAS*, **433**, L59
- Patton, D. R., Qamar, F. D., Ellison, S. L., et al. 2016, *MNRAS*, **461**, 2589
- Patton, D. R., Wilson, K. D., Metrow, C. J., et al. 2020, *MNRAS*, **494**, 4969
- Paudel, S., Duc, P. A., & Ree, C. H. 2015, *AJ*, **149**, 114
- Paudel, S., Smith, R., Yoon, S. J., Calderón-Castillo, P., & Duc, P.-A. 2018, *ApJS*, **237**, 36
- Perepelitsyna, Y. A., Pustilnik, S. A., & Kniazev, A. Y. 2014, *Astrophys. Bull.*, **69**, 247
- Privon, G. C., Stierwalt, S., Patton, D. R., et al. 2017, *ApJ*, **846**, 74
- Pustilnik, S. A., & Martin, J. M. 2016, *A&A*, **596**, A86
- Pustilnik, S. A., & Tepliakova, A. L. 2011, *MNRAS*, **415**, 1188
- Pustilnik, S. A., Perepelitsyna, Y. A., & Kniazev, A. Y. 2016, *MNRAS*, **463**, 670
- Rich, R. M., Collins, M. L. M., Black, C. M., et al. 2012, *Nature*, **482**, 192
- Rojas, R. R., Vogeley, M. S., Hoyle, F., & Brinkmann, J. 2005, *ApJ*, **624**, 571
- Schlafly, E. F., & Finkbeiner, D. P. 2011, *ApJ*, **737**, 103
- Schlegel, D. J., Finkbeiner, D. P., & Davis, M. 1998, *ApJ*, **500**, 525
- Scudder, J. M., Ellison, S. L., Torrey, P., Patton, D. R., & Mendel, J. T. 2012, *MNRAS*, **426**, 549
- Shah, E. A., Kartaltepe, J. S., Magagnoli, C. T., et al. 2022, *ApJ*, **940**, 4
- Stierwalt, S., Besla, G., Patton, D., et al. 2015, *ApJ*, **805**, 2
- Sun, J., Barger, K. A., Frinchaboy, P. M., & Pan, K. 2020, *ApJ*, **894**, 57
- Swaters, R. A., van Albada, T. S., van der Hulst, J. M., & Sancisi, R. 2002, *A&A*, **390**, 829
- Toomre, A., & Toomre, J. 1972, *ApJ*, **178**, 623
- Torrey, P., Cox, T. J., Kewley, L., & Hernquist, L. 2012, *ApJ*, **746**, 108
- Tully, R. B., Rizzi, L., Dolphin, A. E., et al. 2006, *AJ*, **132**, 729
- Venhola, A., Peletier, R., Laurikainen, E., et al. 2019, *A&A*, **625**, A143
- Woods, D. F., Geller, M. J., Kurtz, M. J., et al. 2010, *AJ*, **139**, 1857
- Zibetti, S., Charlot, S., & Rix, H.-W. 2009, *MNRAS*, **400**, 1181